ORGANOMETALLICS

pubs.acs.org/Organometallics Article

Fe(III) Bis-Alkynyls Supported by the TIM Macrocycle: Molecular and Electronic Structures and Altering the Nature of Charge Transfer Transitions through Reduction

Prakhar Gautam, Reese A. Clendening, Andrew T. Poore, Shiliang Tian, and Tong Ren*

Cite This: *Organometallics* 2024, 43, 695−705 Read Online

ACCESS | Metrics & More | Article Recommendations | Supporting Information

ABSTRACT: The bis-alkynyl complexes based on Fe^{III}(TIM) (TIM = 2,3,9,10-tetramethyl-1,4,8,11-tetraazacyclotetradeca-1,3,8,10-tetraene) are reported herein. A modified synthesis of *trans*-[Fe(TIM)Cl_2]PF_6 ([**1**]PF_6) in a 90% yield was developed. The reaction between [**1**]PF_6 and LiC_2R (R = Ph, $SiEt_3$, or Si^iPr_3) resulted in the bis-alkynyl complexes, *trans*-[Fe(TIM)$(C_2R)_2$]PF_6, in good yields, 43% for **2** (R = Ph), 29% for **3** (R = $SiEt_3$), and 18% for **4** (R = Si^iPr_3). X-ray diffraction studies yielded molecular structures of complexes **1**−**3**, which feature a tightened Fe−N_4 coordination in comparison with analogous Fe-(cyclam) complexes. Electron paramagnetic resonance studies confirmed that the complex ions [Fe(TIM)Cl_2]$^+$ and [Fe(TIM)$(C_2R)_2$]$^+$ are low-spin d^5 species with $S = 1/2$ ground states. Electronic absorption spectra of bis-alkynyl complexes **2**−**4** all feature intense LMCT (π(C≡C) → dπ(Fe)) bands in the visible region, and the assignment was supported by the time-dependent density functional theory analysis. These complexes undergo multiple one-electron redox processes, and the first one-electron reduction is reversible in all four complexes and assigned as an Fe(+3/+2) couple. Spectroelectrochemical studies of **1** and **2** reveal that the first one-electron reduction leads to the emergence of intense metal-to-ligand charge transfer (dπ(Fe) → π^*(α-diimine)) bands and the concurrent disappearance of the ligand-to-metal charge transfer bands.

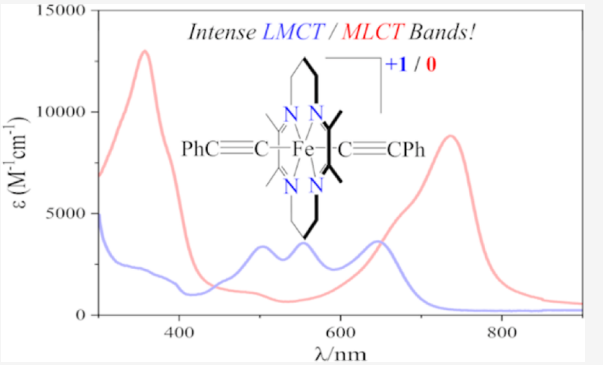

INTRODUCTION

Recent studies of 3d metal complexes supported by tetra/tri-imine macrocycles have offered a few surprises. Notably, the Hess group has utilized $Co^{III}(Mabiq)^{2+}$ (I in Scheme 1) to promote electrochemical hydrogen production[1] and $Co^{III}(Mabiq)Cl_2$ to catalyze C3 and N alkylation of indoles and indazoles with styrene through a visible-light-induced homolysis.[2] Through a collaboration with the laboratory of Vura-Weis, we disclosed a long-lived metal-to-ligand charge transfer (MLCT) state (τ = 1.25 *ns*) in Fe(HMTI)$(CN)_2$ (II in Scheme 1, HMTI = 5,5,7,12,12,14-hexamethyl-1,4,8,11-tetraazacyclotetradeca-1,3,8,10-tetraene).[3] The potential for ligand noninnocence through storing electrons in the α-diimine units of the TIM macrocycle (TIM = 2,3,9,10-tetramethyl-1,4,8,11-tetraazacyclotetradeca-1,3,8,10-tetraene) was demonstrated in the study of Fe(TIM) complexes.[4−6] In turn, Fe^{II}(TIM) was used to probe the redox noninnocence of nitrosoarene ligands.[7] During the investigation of the reaction between electron-rich alkynes, HC_2Y (Y = 4-*N*,*N*-dimethylaniline (DMAP), ferrocene (Fc)) and [Co(TIM)X_2]$^+$ (III), an unusual aza-cobalt-cyclobutene was formed from the [2 + 2] addition of the terminal alkyne to a Co−N bond, which was aided by a formal two-electron donation through the deprotonation of one of the TIM's methyl groups.[8,9] These findings hint at the potential for new reactivity and novel electronic properties to be elicited from the 3d metal complexes of tetra/tri-imine macrocycles.

Scheme 1. Unique Tetra/Tri-imine Complexes: (I) $Co^{III}(Mabiq)X_2$; (II) $Fe^{II}(HMTI)(CN)_2$; and (III) [$Co^{III}(TIM)X_2$]$^+$

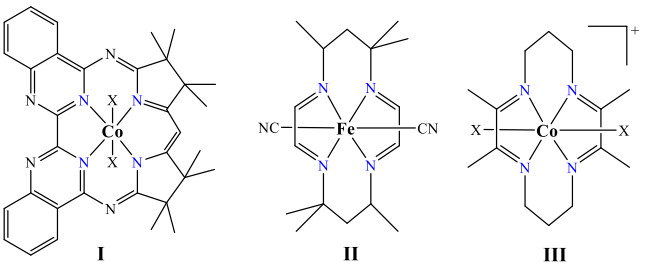

I II III

Received: January 15, 2024
Revised: February 22, 2024
Accepted: February 23, 2024
Published: March 6, 2024

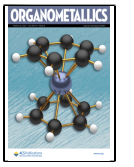

https://doi.org/10.1021/acs.organomet.4c00015
Organometallics 2024, 43, 695−705

The studies of iron alkynyl compounds have significantly enriched the chemistry of metal alkynyl compounds.[10] It is noteworthy that earlier contributions include σ-alkynyl complexes of $Fe_2(CO)_n$ (n = 5 and 6) and the coupling reactivities therein by Carty and co-workers,[11,12] the first demonstration of [2 + 2] cycloaddition and subsequent retroelectrocyclization of TCNE on the acetylide bond by the laboratory of Bruce,[13] and rigid rod iron-containing polyynes by the laboratory of Lewis.[14,15] Numerous examples of facile electron delocalization across a polyyne or carbon-rich bridge between two $CpFe^{II}$ termini have been disclosed by the laboratory of Lapinte on the basis of Fe^{II}−Fe^{III} mixed valency.[16,17] Low ohmic wire characteristic was demonstrated with the break-junction STM measurement of a number of Fe−C_4−Fe-type molecules.[18] Reflecting the heightened interest in organometallic catalysis, recent years have witnessed some interesting cases with Fe alkynyls as either a precatalyst or a reaction intermediate.[19−21]

Our laboratory has studied a number of 3d metal alkynyl complexes supported by both cyclam (1,4,8,11-tetraazacyclotetradecane) and its C-substituted derivatives during the past decade.[22,23] While interesting structural features were observed, the conjugation along the metal−alkynyl backbone was weak at best.[24] The investigation of the $[Fe^{III}(HMTI)(C_2R)_2]^+$-type complexes revealed that the dπ(Fe) → π*(α-diimine) interaction is substantial due to the enhanced π-acidity of the unsaturated HMTI.[25,26] Subsequent study of the $[Y−Y]^+$ mixed valency in the $[Fe^{III}(HMTI)(C_2Y)_2]^+$-type complexes (Y = DMAP and Fc) revealed facile hole delocalization across the $−C_2−Fe^{III}−C_2−$ backbone, further proving the significance of the π-acidity of HMTI in enabling metal−alkynyl conjugation.[27] Nonetheless, further investigation of electronic and optical properties of Fe(HMTI) species is hindered by their low-yielding syntheses, which are generally based on aerobic dehydrogenation of the corresponding Fe(HMC) complexes (HMC = 5,5,7,12,12,14-hexamethyl-1,4,8,11-tetraazacyclotetradecane).[28] It is noteworthy that $[Fe^{II}(TIM)(NCCH_3)_2](PF_6)_2$ can be prepared on a multigram scale in a single step[4] and quantitatively converted to $[Fe^{III}(TIM)Cl_2]PF_6$, and the latter is a potential entry point for Fe^{III}(TIM) organometallic complexes. Described in this contribution are the bis-alkynyl complexes based on Fe^{III}(TIM) (vide infra) and their molecular and electronic structures.

RESULTS AND DISCUSSION

Synthesis. Previously, complex *trans*-$[Fe(TIM)Cl_2]PF_6$ ($[\mathbf{1}]PF_6$) was prepared from treating $[Fe^{II}(TIM)(NCCH_3)_2](PF_6)_2$ with HCl in a reported yield of 91%.[29] Because of the difficulty in reproducing the above-mentioned procedure, $[\mathbf{1}]PF_6$ is generated in comparable yield (90%) via a slow addition of $FeCl_3$ to a solution of $[Fe(TIM)(NCCH_3)_2](PF_6)_2$. As shown in Scheme 2, the reaction between $[\mathbf{1}]PF_6$ and LiC_2R (R = Ph, $SiEt_3$, or Si^iPr_3), conducted at either −78 or 21 °C, produces the respective bis-alkynyl complexes, *trans*-$[Fe(TIM)(C_2Ph)_2]PF_6$ ($[\mathbf{2}]PF_6$), *trans*-$[Fe(TIM)(C_2SiEt_3)_2]PF_6$ ($[\mathbf{3}]PF_6$), and *trans*-$[Fe(TIM)(C_2Si^iPr_3)_2]PF_6$ ($[\mathbf{4}]PF_6$) in high in situ yields. The existence of monoalkynyl and other unidentified byproducts necessitates purification over silica using CH_2Cl_2/acetone, affording the desired complexes in moderate yields (18−43%). Efforts to achieve $[\mathbf{2}]PF_6$−$[\mathbf{4}]PF_6$ directly from the reaction between $[Fe(TIM)(NCCH_3)_2](PF_6)_2$ and the appropriate LiC_2R reagent were hampered by the presence of many byproducts and difficulty in purification.

Scheme 2. Syntheses of Complexes $[\mathbf{2}]^+$−$[\mathbf{4}]^+$[a]

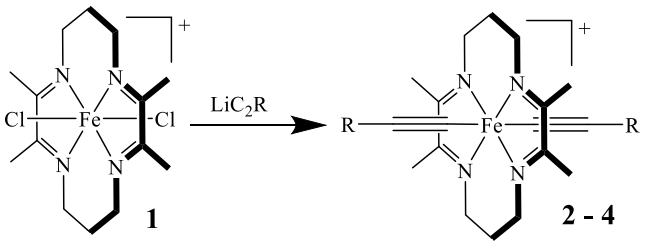

[a]Conditions: LiC_2R; THF; −78 °C, R = Ph (**2**), $SiEt_3$ (**3**), or $LiC_2Si^iPr_3$ (**4**); THF; 0 °C.

Although the yields are not impressive, the synthesis of $[Fe(TIM)(C_2R)_2]^+$ is based on a one-step reaction of $[\mathbf{1}]PF_6$ with the appropriate LiC_2R, a significant improvement over that of Fe(HMTI) alkynyl species.[25−27] For the latter, the oxidative dehydrogenation of the saturated macrocycle in the Fe(HMC) precursor complex is required and is achieved in situ by the addition of excess *n*-butyllithium/HC_2R followed by the subsequent exposure of the reaction mixture to air. However, the tetra-imine nature of the TIM ligand in $[\mathbf{1}]PF_6$ eliminates the need for both the oxidative dehydrogenation step and the ensuing purification to remove the byproducts. For instance, while *trans*-$[Fe(HMTI)(C_2SiEt_3)_2]ClO_4$ was isolated in a yield of 9%,[25] $[\mathbf{3}]PF_6$ was prepared in a yield of 29%.

Molecular Structures. The molecular structures of $[\mathbf{1}]PF_6$, $[\mathbf{2}]PF_6$, and $[\mathbf{3}]NTf_2$ were determined via single-crystal X-ray diffraction (Figure 1). Selected bond lengths are listed in Table 1, and the details of data collection and structure refinement are provided in Table S1 of the Supporting Information.

A pseudo-octahedral geometry is adopted for the Fe^{3+} center in all complexes, wherein the TIM macrocycle occupies the equatorial sites and chloro or alkynyl ligands occupy the *trans*-axial sites. The N═C bond lengths in $[\mathbf{1}]^+$−$[\mathbf{3}]^+$ are within a narrow range of 1.286(4)−1.298(6) Å similar to those in $[Fe(TIM)(NCCH_3)_2]^{2+}$ (1.287−1.297 Å), confirming the retention of α-diimine units in TIM upon the complexation. Further supporting a neutral α-diimine backbone, the lengths of bridging C−C bonds of the α-diimines for $[\mathbf{1}]^+$ (C1−C2), $[\mathbf{2}]^+$ (C10−C11), and $[\mathbf{3}]^+$ (C10−C11) range from 1.457(7)−1.475(5) Å, similar to those in the comparable Co^{III}(TIM) and Fe^{III}(HMTI) complexes.

A comparison of the structures of analogous Fe(TIM) and Fe(HMTI) species reveals only subtle variations in the geometry of the α-diimine units. Specifically, $[\mathbf{2}]^+$ and $[\mathbf{3}]^+$ have bond lengths of 1.457(7) and 1.468(2) Å, respectively, whereas the corresponding bond length in $[Fe(HMTI)(C_2Ph)_2]^+$ is 1.442(3) Å for the bridging C−C bond of the α-diimines. A similar comparison can be made between $[\mathbf{1}]^+$ and $[Fe(HMTI)Cl_2]^+$ (see Table S2). This provides evidence that the methyl substituents on TIM have a minimal influence on the Fe−N_4 coordination sphere, resulting in a high degree of structural similarity between Fe(TIM) and Fe(HMTI) analogues. Furthermore, the metal ion has a minimal effect on the size of the TIM macrocycle, as corroborated by the analysis of the corresponding bond lengths in $[Co(TIM)(C_2Ph)_2]^+$.[30] For $[Co(TIM)(C_2Ph)_2]^+$, the C−C bond length ranges from 1.385(4) to 1.503(5) Å and the C═N bond lengths range

https://doi.org/10.1021/acs.organomet.4c00015
Organometallics 2024, 43, 695−705

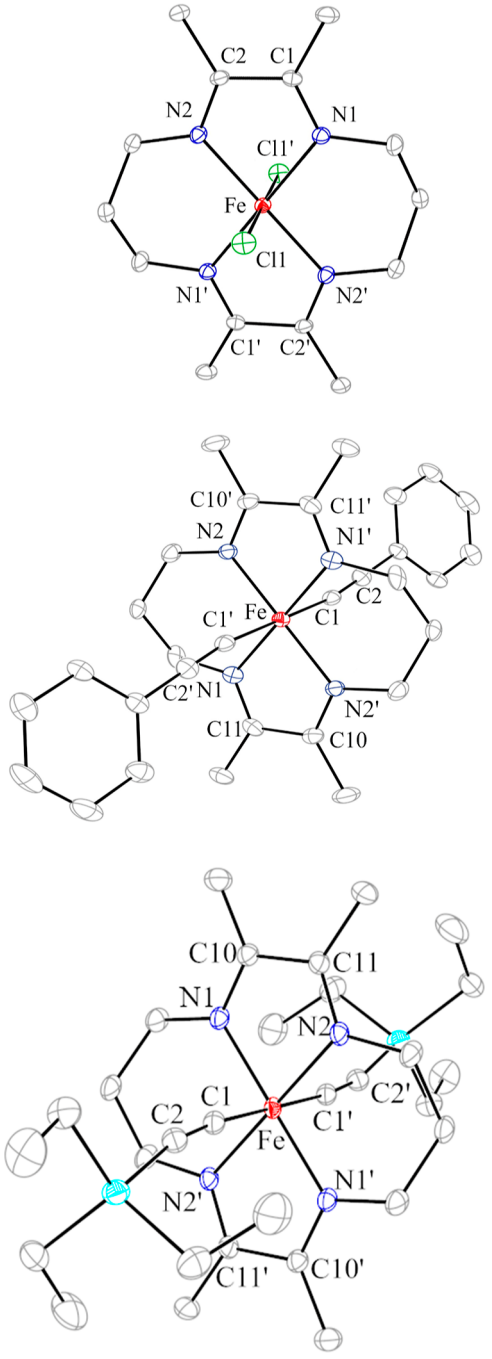

Figure 1. ORTEP plot of $[1]^+$ (top), $[2]^+$ (middle), and $[3]^+$ (bottom) at the 30% probability level. Hydrogen atoms and the counterions are omitted for clarity. A crystallographic center of inversion is situated at the Fe center in all three cases (space group: $P\bar{1}$ for $[1]^+$, and $P2_1/n$ for $[2]^+$ and $[3]^+$).

from 1.273(4) to 1.322(4) Å, both of which are similar to those of $[2]^+$. However, a shorter Co−N bond length (1.924−1.928 Å) is observed for $[Co(TIM)(C_2Ph)_2]^+$, likely due to the smaller radius of Co^{III}.[31]

Also, there is no discernible influence of the methyl substituents on the Fe−N bond lengths. The average Fe−N bond length in $[1]^+$ is 1.942[4] and is experimentally identical to the Fe−N_{av} distance in $[Fe(HMTI)Cl_2]^+$ (1.942[3]) (Å). However, as discussed below, the introduction of electron-donating methyl substituents to the α-diimine units does have a significant influence on the relative π-acidity of the TIM macrocycle when compared to HMTI, where all six methyl substituents are *C*-bound and away from the α-diimine units.

UV−Vis Spectroscopic Analysis. UV−vis absorption spectra for complexes $[1]PF_6$−$[4]PF_6$ are shown in Figure 2

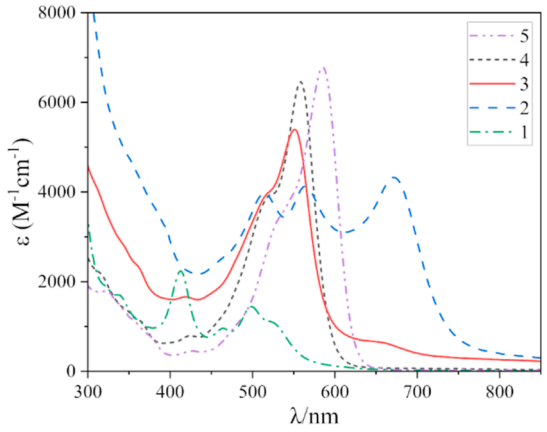

Figure 2. Absorption spectra of $[1]PF_6$, $[2]PF_6$, $[3]PF_6$, $[4]PF_6$, and $[5]ClO_4$ in CH_2Cl_2.

Table 2. Characteristics of Absorption Spectra of Complexes $[1]PF_6$−$[4]PF_6$ and $[5]ClO_4$ in CH_2Cl_2

	$[1]PF_6$	$[2]PF_6$	$[3]PF_6$	$[4]PF_6$	$[5]ClO_4$
λ_{max}	494, 413	670, 564, 514	551 (513, sh)	559 (517, sh)	584 (531, sh)
ν (cm^{-1})	20 200, 24 200	14 900, 4100, 3900	18 100	17 900	17 100
ε (M^{-1} cm^{-1})	1600, 2200	4300	5400	6500	6700

and relevant parameters are listed in Table 2. The spectrum of $[Fe^{III}(HMTI)(C_2SiEt_3)_2]ClO_4$ ($[5]ClO_4$) is also included for comparison. Complex $[1]PF_6$ displays several weak absorption bands centered around 494 nm with an extinction coefficient of 1600 M^{-1} cm^{-1}, followed by a sharp peak at 413 nm (2200

Table 1. Selected Bond Lengths (Å) for $[1]^+$, $[2]^+$, $[3]^+$, $[Fe(HMTI)(C_2Ph)_2]^+$,[26] and $[Co(TIM)(C_2Ph)_2]^+$[30]

	$[1]^+$	$[2]^+$	$[3]^+$	$[Fe(HMTI)(C_2Ph)_2]^+$	$[Co(TIM)(C_2Ph)_2]^+$
M−N	1.936(3)−1.947(3)	1.927(4)−1.933(4)	1.9296(13)−1.9330(13)	1.926(1)−1.938(1)	1.899(7)−1.933(7)
C−C[a]	1.475(5)	1.457(7)	1.468(2)	1.442(3)	1.385(4)−1.503(5)
N=C	1.286(4)−1.294(4)	1.293(6)−1.298(6)	1.295(2)−1.296(2)	1.282(2)−1.286(2)	1.273(4)−1.322(4)
C≡C		1.204(6)	1.221(8)	1.207(2)−1.208(2)	1.192(18)−1.217(18)
M−C/Cl	2.2518(7)	1.969(5)	1.9534(16)	1.945(2)−1.949(2)	1.918(14)−1.929(14)

[a]Internal C−C bonds of the α-diimines.

https://doi.org/10.1021/acs.organomet.4c00015
Organometallics 2024, 43, 695−705

M^{-1} cm^{-1}). These weak, overlapping charge transfer bands are attributed to a combination of excitations from Fe^{III}/Cl^- to the empty π^* of the α-diimines and from the lone pair orbitals of the axial chloro ligands to the half-filled Fe^{III} dπ orbital based on the density functional theory (DFT) analysis (see below).

In contrast to [**1**]PF_6, the bis-alkynyl Fe(TIM) complexes, [**2**]PF_6–[**4**]PF_6, display intense visible peaks. The spectrum of complex [**2**]PF_6 features three pronounced peaks centered at 514, 564, and 670 nm, a feature that is common among bis-phenylacetylide Fe^{III} complexes of cyclam[32] and HMTI.[26] Similar to [**5**]ClO_4, complexes [**3**]PF_6 and [**4**]PF_6 display both intense bands at 551 and 559 nm, respectively, and discernible shoulders at higher energies (513 nm for [**3**]PF_6 and 517 nm for [**4**]PF_6). These intense bands are assigned as ligand-to-metal charge transfer (LMCT) transitions from π(C≡C) to dπ(Fe) based on literature precedent, which is corroborated here computationally (vide infra). The irregularly spaced charge transfer bands for [**2**]PF_6 are likely due to vibronic couplings, ascribed to either aromatic ν(C═C) stretching modes or potential deformation of the phenyl ring. Interestingly, the LMCT peak in [**3**]PF_6 has been blue-shifted from that in [**5**]ClO_4 by *ca.* 1000 cm^{-1} or 0.13 eV. Likewise, a blue shift of similar magnitude in the LMCT peaks of [**2**]PF_6 from those of $[Fe^{III}(HMTI)(C_2Ph)_2]^+$ is noted as well (see Figure S2).

Electrochemistry. Voltammetric properties of complexes [**1**]PF_6–[**4**]PF_6 were examined and their cyclic voltammograms and differential pulse voltammograms are shown in Figure 3. The electrode potential data are listed in Table 3

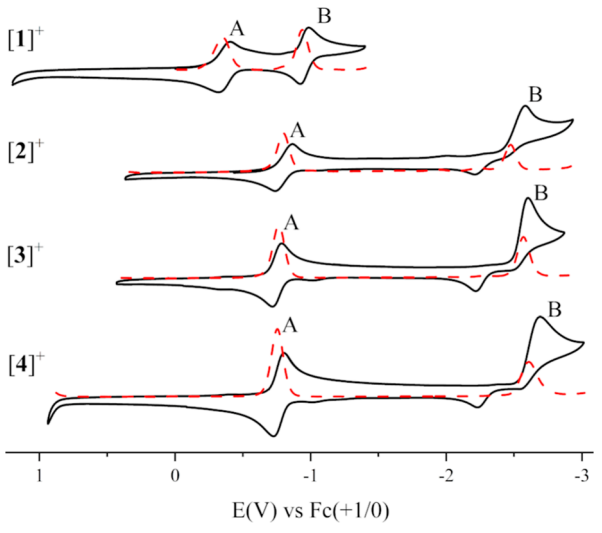

Figure 3. CV (solid black) and DPV (red dash) traces of [**1**]$^+$ (top), [**2**]$^+$ (middle top), [**3**]$^+$ (middle bottom), and [**4**]$^+$ (bottom) recorded in 0.1 M solutions of *n*-Bu_4NPF_6 in CH_2Cl_2 ([**1**]$^+$) or THF ([**2**]$^+$–[**4**]$^+$) at a scan rate of 0.10 V/s. At cathodic potentials, reduction of the Fe^{III} center (A) and the TIM (B) is observed.

along with those of [**5**]$^+$. Because of the difference in solubility, the voltammograms of [**1**]$^+$ were recorded in CH_2Cl_2 while those of [**2**]$^+$–[**4**]$^+$ are reported in THF. In the anodic region, the three bis-alkynyl complexes exhibit an irreversible oxidation that is assigned to an Fe(+4/+3) couple based on analogous Fe(HMC) alkynyl complexes (Figure S1).[26] In the cathodic region, complexes [**1**]$^+$–[**4**]$^+$ undergo two reduction events. The initial reduction is reversible and assigned as an Fe(+3/+2) couple. The Fe(+3/+2) couples of the bis-alkynyl

Table 3. Electrode Potentials (V, vs $Fc^{+1/0}$)

complex	$E_{1/2}$ ($Fe^{3+/2+}$)	$E_{p,c}$ ($TIM^{0/-1}$)
[**1**]$^+$(CH_2Cl_2)	−0.36	−0.96
[**2**]$^+$(THF)	−0.80	−2.5
[**3**]$^+$(THF)	−0.75	−2.6
[**4**]$^+$(THF)	−0.76	−2.7
[**5**]$^+$(THF)	−0.56	−2.4[a]

[a]Reduction of HMTI.

complexes are shifted by *ca.* −0.40 V from that of [**1**]$^+$, as the result of the alkynyls being much stronger donors than the chloro ligand. The second reduction is attributed to the reduction of TIM based on the analysis of [Fe(TIM)-$(NCCH_3)_2$]$(PF_6)_2$ by Wieghardt and co-workers.[6] While the TIM-based reduction in [**1**]$^+$ at −0.96 V is reversible, the same reductions in [**2**]$^+$–[**4**]$^+$ are significantly cathodic-shifted (*ca.* −2.5 V) and irreversible. A smaller wave appears at a more anodic potential than for $E_{p,c}$ (B) on the return sweep in [**2**]$^+$–[**4**]$^+$, which is indicative of the disintegration of the complex upon second reduction, plausibly via dissociation of an alkynyl ligand.

When comparing [**2**]$^+$ and [**3**]$^+$ to their respective HMTI-based analogues, $[Fe(HMTI)(C_2Ph)_2]^+$ and [**5**]$^+$ (Table S3), a cathodic shift of *ca.* 0.2 V is seen for the Fe(+3/+2) couple. This trend holds for the second reduction of the complexes as well, where the ligand reduction for the Fe(TIM) species occurs at a more cathodic potential (*ca.* −0.2 V) than for the Fe(HMTI) analogue. The contrast highlights that while both TIM and HMTI macrocycles stabilize Fe dπ orbitals through their π^*(α-diimine) orbitals, the methyl groups on the α-diimines of TIM render TIM more electron-rich than HMTI.

Spectroelectrochemistry. Spectroelectrochemical (SEC) analysis is a powerful tool for the in-depth understanding of the electronic structures of Fe-tetraimine complexes. Access to the spectrum of $[Fe(HMTI)(CN)_2]^{-1}$ helped to ascertain the MLCT absorption in the transient spectra of Fe(HMTI)-$(CN)_2$.[3] The extraction of the $[Fe(HMTI)(C_2Y)_2]^{+2}$ spectrum allowed the establishment of an IVCT band associated with the $[Y-Y]^+$ pair that is consistent with a highly delocalized class II mixed valency.[27]

As described in the Experimental Section, the SEC measurement of [**1**]$^+$ was carried out in CH_2Cl_2 due to solubility consideration, while that of [**2**]$^+$ was performed in THF. Upon the reduction from [**1**]$^+$ to [**1**]^0 (Figure 4 and Table 4), two new MLCT bands grow at ca. 491 nm and ca. 569 nm, and a broad band grows at ca. 753 nm. The broad band is assigned as an MLCT and attributed to a transition from the now filled dπ orbital of the Fe^{II} to the π^*(diimine). The higher energy bands at ca. 569 and 491 nm are attributed predominantly to the ligand-to-ligand charge transfer (LLCT), from the filled π orbital(s) of the chloro ligands to the π^*(diimine), though a contribution from a higher energy MLCT cannot be excluded. These assignments are discussed further in the Computational Analysis section.

The reasonably reversible second reduction observed in the cyclic voltammetry (CV) of **1** suggested the feasibility of analyzing [**1**]$^{1-}$ through SEC. Indeed, a further reduction from [**1**]^0 to [**1**]$^{1-}$ results in the emergence of an intense band at ca. 527 nm as well as a broad peak at ca. 668 nm, presumably due to the formal population of the lowest π^*(diimine). As discussed in more detail in the Computational Analysis section, these bands are probably best attributed to excitations from

https://doi.org/10.1021/acs.organomet.4c00015
Organometallics 2024, 43, 695−705

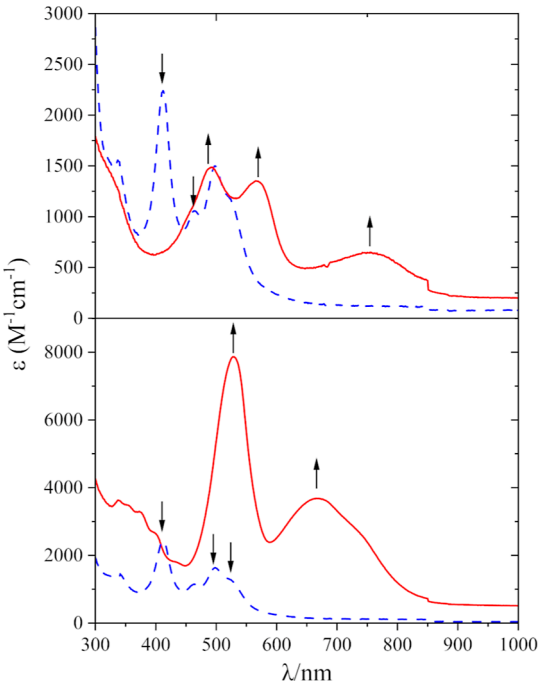

Figure 4. Top window: UV−vis−NIR SEC of $[1]^+$ (blue, 5 mM) to $[1]^0$ (red) upon reduction. Bottom window: further reduction from $[1]^+$ (blue) to $[1]^{1-}$ (red) in CH_2Cl_2 (0.1 M n-Bu_4NPF_6).

Table 4. Characteristics of Absorption Spectra of Complexes $[1]^+$ and $[2]^+$ Following Their Respective Reductions

	$[1]^0$	$[2]^0$	$[1]^{1-}$
λ_{max}	491, 569, 753	357, 735	527, 668
ν (cm^{-1})	20 300, 17 500, 13 300	28 000, 13 600	18 900, 14 900
ε (M^{-1} cm^{-1})	1400, 1300, 600	13 300, 9000	7900, 3700

this newly populated orbital to higher energy π^* orbitals, although the lower energy band appears to have appreciable LMCT character as well.

Upon the reduction from $[2]^+$ to $[2]^0$, the structured LMCT bands between 450 and 650 nm are replaced by two more intense peaks at 357 and 735 nm (Figure 5). The band at 735 nm is attributed to the MLCT from the filled t_{2g} to the

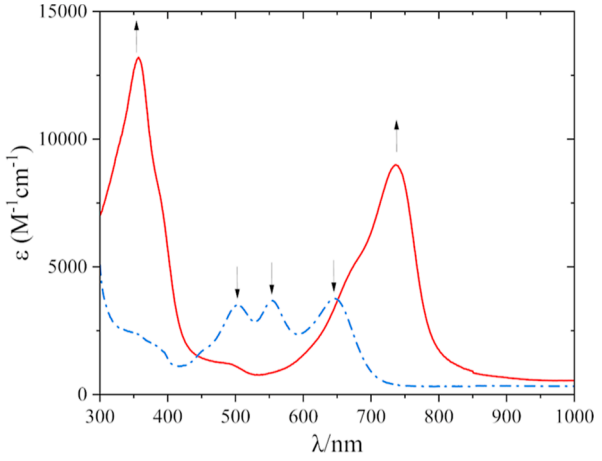

Figure 5. UV−vis SEC of $[2]^+$ (blue) accessing the first reduction to form $[2]^0$ (red) in THF (0.1 M n-Bu_4NPF_6).

π^*(diimine) and verified by time-dependent DFT (TD-DFT) analysis (vide infra). The high-energy charge transfer at ca. 357 nm is attributed to the MLCT transition as well, predominantly from the highest filled dπ orbital of the Fe^{II} to a high lying $\pi^*(C_2Ph)$ orbital. A qualitative comparison with the Fe(HMTI) analogue (Figure S3) shows a striking similarity in the charge transfer bands of the two reduced species. TD-DFT analysis confirms the charge transfer bands that appear for $[2]^0$ and the analogous Fe(HMTI) complex are MLCT bands and have similar excitation trends, highlighting the role the α-diimine units played in conjunction with the electron-deficient Fe center. Further reduction of $[2]^0$ to $[2]^{1-}$ (Figure S4) is irreversible and did not yield any reasonable quantitative return. In contrast, oxidation of $[2]^0$ back to $[2]^+$ regenerates the original spectrum (Figure S5).

Electron Paramagnetic Resonance Characterization. To experimentally determine the ground state of the bis-alkynyl $[Fe(TIM)(C_2R)_2]^+$ complexes, continuous-wave (CW) X-band electron paramagnetic resonance (EPR) was conducted at 8 K using a 2 mM solution of $[Fe(TIM)(C_2R)^2]^+$ in a 1:1 mixture of acetonitrile and toluene. The resulting spectra were analyzed and simulated utilizing EasySpin (Figure 6), with the fitting parameters listed in Table 5.[33]

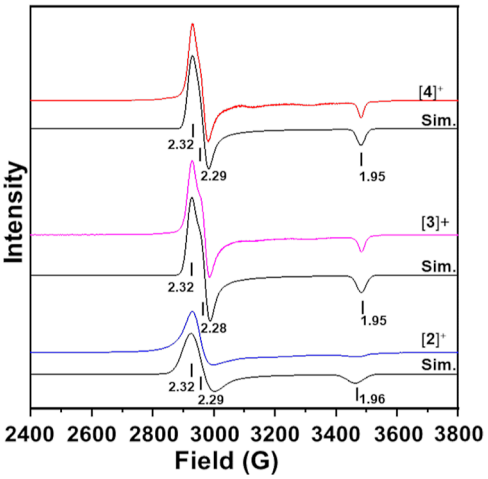

Figure 6. CW X-band EPR spectra of $[2]^+$−$[4]^+$ in a 1:1 acetonitrile/toluene solution. EasySpin simulations are presented below their respective spectra (black) with g values indicated. Conditions: temperature of 8 K, modulation amplitude of 2 G, microwave power of 10.0 mW, and microwave frequency of ∼9.50 GHz.

Table 5. EPR Parameters and Spin Analysis for $[1]^+$−$[4]^+$

complex	g values	Σg^2
$[1]^+$	2.4097	14.87
	2.3106	
	1.9299	
$[2]^+$	2.3162	14.46
	2.2934	
	1.9595	
$[3]^+$	2.3204	14.40
	2.2848	
	1.9487	
$[4]^+$	2.3181	14.40
	2.2872	
	1.9484	

https://doi.org/10.1021/acs.organomet.4c00015
Organometallics 2024, 43, 695−705

EPR simulation of $[\mathbf{1}]^+$−$[\mathbf{4}]^+$ shows that all complexes are axial low-spin $S = 1/2$ Fe^{III} species (Figure 6), with the exception of complex $[\mathbf{1}]^+$ displaying a slightly more rhombic signal (Figure S9).[34] According to the Griffith theory, first developed for low-spin ferric porphyrin complexes, a large g_{max} ($g \approx 3$) and a $\Sigma g^2 = 16$ are typical for a $(d_{xy})^2(d_{xz},d_{yz})^3$ ground state, whereas a $(d_{xz},d_{yz})^4(d_{xy})^1$ ground state usually has an axial EPR spectrum with a $g_{max} < 2.6$ and $\Sigma g^2 < 16$.[35−39] The g values for the alkynyl complexes $[\mathbf{2}]^+$−$[\mathbf{4}]^+$ were found to be in the same range as seen for the previously reported Fe(HMTI) complexes,[27] with a slightly higher Σg^2 values ranging from 14.40 to 14.46 (Table 5). This suggests that the alkynyl complexes $[\mathbf{2}]^+$−$[\mathbf{4}]^+$ have a $(d_{xz},d_{yz})^4(d_{xy})^1$ ground state. This assignment is consistent with the short Fe−N bond distances observed in the crystal structures (Table 1). The α-diimines on the TIM macrocycle are effective π acceptors, allowing sufficiently stabilized dπ orbitals of the Fe(III) center and resulting in the lower energies of the d_{xz} and d_{yz} orbitals.

Computational Analysis. To gain an in-depth understanding of both ground-state electronic structures and the major vis−NIR absorption characteristics, spin-polarized (unrestricted) DFT and TD-DFT calculations were performed for **1**, **2**, and their reduced derivatives using the Gaussian 16 suite.[40] The X-ray structures of $[\mathbf{1}]^+$ and $[\mathbf{2}]^+$ served as the starting geometries for the optimized model complexes $[\mathbf{1}']^+$ and $[\mathbf{2}']^+$, respectively, which are chemically identical to the crystallographically determined structures of these cations (counteranions were omitted). As noted in the EPR study above, both $[\mathbf{1}]^+$ and $[\mathbf{2}]^+$ are best described as the low-spin d^5 species. Hence, a doublet spin state was used for both $[\mathbf{1}']^+$ and $[\mathbf{2}']^+$. The structures of $[\mathbf{1}']^0$ and $[\mathbf{2}']^0$ were optimized from the converged coordinates of $[\mathbf{1}']^+$ and $[\mathbf{2}']^+$, following the addition of a single electron to yield the neutral species. The $S = 0$ spin state was assumed, consistent with other Fe^{II}(TIM) complexes.[4,6,29] The geometry of $[\mathbf{1}']^{-1}$ was likewise optimized from that of $[\mathbf{1}']^0$ (after the appropriate modification of charge) with an assumed spin state of $S = 1/2$. DFT and TD-DFT for $[\mathbf{2}']^{-1}$ were not attempted due to the irreversible nature of this reduction.

The unrestricted nature of the calculation leads to some spin contamination, and thus the α and β orbitals of $[\mathbf{1}']^+$ and $[\mathbf{2}']^+$ do not match perfectly. Nonetheless, a reasonable ground state emerges in which these are best described as $Fe^{III}(TIM^0)$ complexes, in agreement with the EPR data presented above. Thus, the unoccupied β orbital, which has no similarly unoccupied α counterpart for $[\mathbf{1}']^+$, is dominated by the iron center (ca. 83% based on a population analysis). However, the highest, singly occupied molecular orbital (α SOMO) of $[\mathbf{1}']^+$ shows a high degree of Cl p_x character (ca. 76% total over both chloro ligands) in addition to the expected Fe d_{xz} character (24%). Moreover, the next four orbitals (α HOMO − 1 to HOMO − 4) are all dominated by the chloride p character (>80%). In contrast, d_{x2-y2}, which is formally nonbonding under the approximate D_{2h} symmetry of the molecule, is represented by α HOMO − 6. It should be noted that because the choice of XY is 45° rotated from the conventional setting (used in the preceding EPR discussion) in DFT calculations, the t_{2g} set consists of d_{xz}, d_{yz}, and d_{x2-y2}, while the e_g set consists of d_{z2} and d_{xy}. The frontier filled molecular orbitals thus contain a very high degree of the chloro character.

In contrast, the lowest unoccupied molecular orbitals (LUMOs) are dominated by the α-diimine moieties and by the metal center. The first of these (α LUMO) is π^*(α-diimine) in character and is nonbonding with respect to the metal center. The α LUMO + 1 is also based on the α-diimines but has the proper symmetry to mix with the Fe d_{xz}. The nature of these orbitals is consistent with that previously reported for Fe(HMTI) complexes.[26] The empty σ-antibonding Fe d_{z2} (a_g) and d_{xy} (b_{1g}) are observed as LUMO + 2 and LUMO + 3, respectively.

The results obtained for $[\mathbf{2}']^+$ mirror those of $[\mathbf{1}']^+$ closely, except that the chloride p-orbital character present in the frontier occupied orbitals is replaced by the more diffused $\pi(C_2Ph)$ orbitals. Additionally, evidence of the stronger donor character of phenylacetylide over chloride may be observed. First, the α SOMO−LUMO gap of $[\mathbf{1}']^+$ (3.78 eV, see Figure 7) is noticeably larger than that of $[\mathbf{2}']^+$ (2.62 eV, see Figure 8), presumably due to the strong π-donating character of C_2Ph in the latter, which elevates the energy of the filled Fe dπ orbitals. The phenylacetylide is also a stronger σ donor than chloride, elevating the unfilled Fe d_{z2} above the Fe d_{xy} for $[\mathbf{2}']^+$.

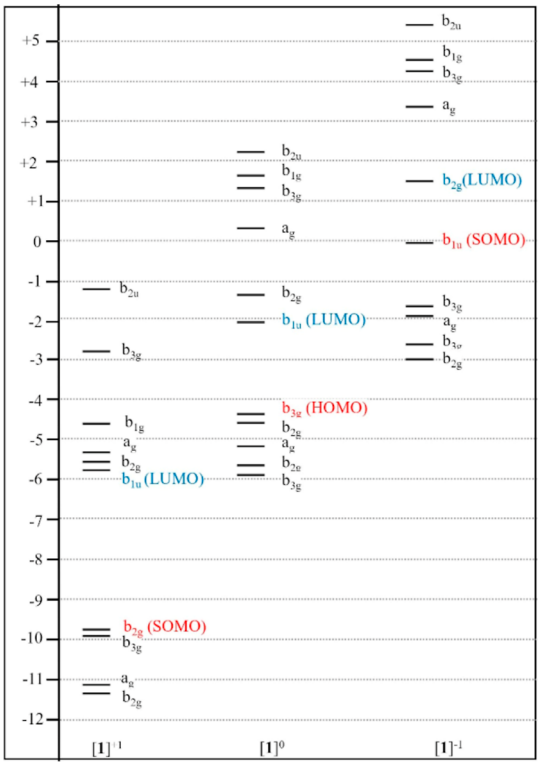

Figure 7. Diagram of relative computed energies of related orbitals for $[\mathbf{1}]^z$. The SOMO/HOMO is indicated in red and the LUMO is indicated in blue. For doublet ($z = +1$ and -1) systems, the α-orbital energies are used.

The addition of a single electron to form $[\mathbf{1}']^0$ and $[\mathbf{2}']^0$ significantly increases the energy of the Fe d orbitals, consistent with the metal-centered reduction to Fe^{II}. The result is that the frontier occupied orbitals of $[\mathbf{1}']^0$ and $[\mathbf{2}']^0$ are now more Fe-based. Indeed, HOMO through HOMO − 2 of $[\mathbf{1}']^0$ is predominantly Fe d_{yz}, d_{xz}, and d_{x2-y2}. These occur in the same order as the HOMO, HOMO − 1, and HOMO − 3 of $[\mathbf{2}']^0$ (the HOMO − 2 is still of the $\pi(C_2Ph)$ character). While the LUMO in each case remains localized on the α-diimine, the LUMO + 1 gains appreciable Fe d_{xz} character (ca. 21% in $[\mathbf{1}']^0$ and 23% in $[\mathbf{2}']^0$) through backbonding with the

https://doi.org/10.1021/acs.organomet.4c00015
Organometallics 2024, 43, 695−705

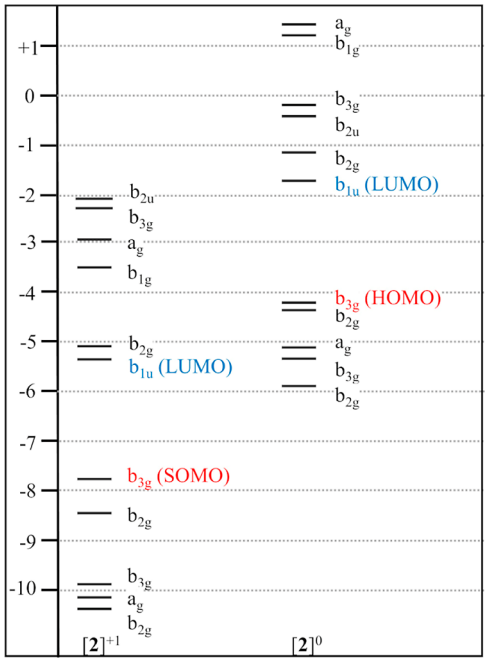

Figure 8. Diagram of relative computed energies of related orbitals for $[2]^z$. The SOMO/HOMO is indicated in red and the LUMO is indicated in blue. For the doublet (z = +1) system, the α-orbital energies are used.

reduced metal center. Selected orbitals for $[2']^0$ have been represented in Figure 9. The reduction also elevates the empty σ-antibonding d orbitals of $[2']^0$, such that the lowest of these (d_{xy}) is not observed until LUMO + 7 (not shown).

Further reduction of **1** should result in the formation of an anionic TIM macrocycle.[6] This is indeed the result obtained for the optimized structure of $[1']^{-1}$, which shows the population of the lowest π^*(diimine) with a single electron as the new SOMO. Otherwise, the frontier molecular orbitals display the same general trends as observed for $[1']^0$, except that their energies are increased by the addition of an electron. It should be noted that a thorough computational analysis of the $[Fe(TIM)]^z$ series (z = +2, +1, 0, and −1) was presented by Hess and Wieghardt,[6] and the general trend of the variation in valence MOs upon reduction is similar to the observation here. However, a more detailed comparison is untenable since the computational models used by Hess and Wieghardt are free of axial ligands.

TD-DFT was conducted to better interpret both the initial absorption spectrum and those obtained via SEC (vide supra). The results for $[2']^+$ match well with those already published for the HMTI analogue.[26] The calculated low-energy spectrum (Figure S13) is dominated by a single transition at 636.99 nm from an occupied β $\pi(C_2Ph)$ orbital to the unoccupied β Fe(d_{yz}). This compares well with the observed lowest energy band (670 nm in CH_2Cl_2). Thus, the original LMCT assignment is confirmed. Weaker transitions predicted at <400 nm (see Table S9) likely contribute to shoulders observable in this region in Figure 2. Notably, the triple-peak nature of the low-energy LMCT manifold seen in Figure 2 is not reproduced computationally. This was also true of the HMTI analogue[26] and suggests that the splitting originates not from the ground state, but instead from vibronic couplings as suggested above.

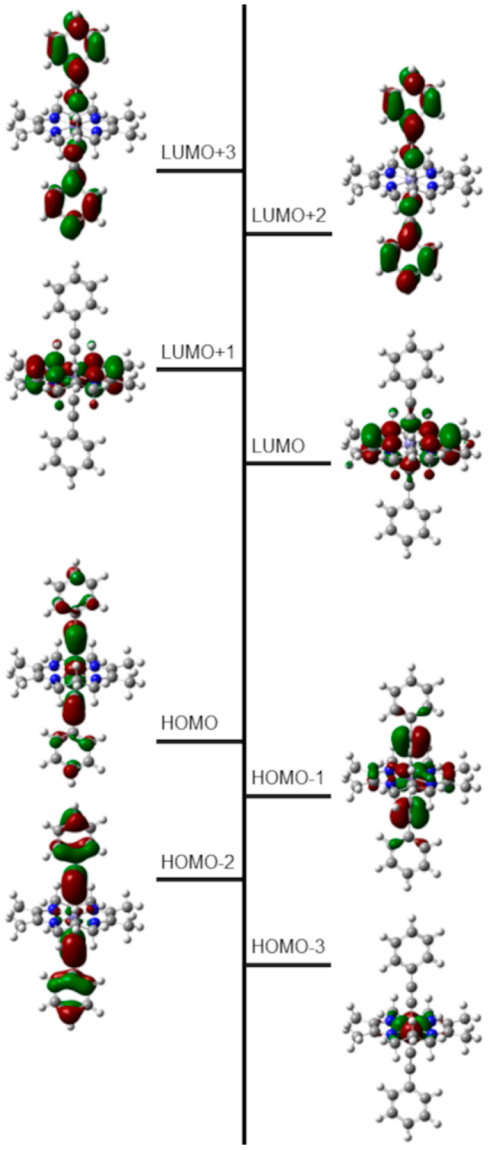

Figure 9. Selected molecular orbital diagrams for $[2]^0$ obtained from DFT calculations, represented at lisovaluel = 0.03.

Assignments in the case of $[1']^+$ are more difficult due to the complexity of the absorption manifold. Indeed, close inspection of Figure 2 suggests the presence of at least four bands between about 400 and 550 nm, each with weak to moderate intensity. It is thus not surprising that six weak-to-moderate transitions are predicted from about 330 to 500 nm (see Table S6). Inspection of the two lowest energies of these (504.87 and 441.02 nm) reveals that they both consist of transitions from filled orbitals of the mixed iron and chloro character to the lowest unoccupied $\pi^*(\alpha$-diimine). These may thus be classified as MLCT for simplicity, but with substantial LLCT. The next transition at 363.57 nm is almost entirely dichloro-to-iron charge transfer (LMCT). The remaining transitions have various mixed characters and consist largely of higher energy LMCT and MLCT/LLCT transitions. Due to both limitations of spin-polarized DFT and the above-mentioned complexity, exact assignments of all bands are not attempted. However, two qualitative observations can be made. First, the overlapping, lower-energy bands may be classified as MLCT in character, with perhaps some admixture of LLCT.

https://doi.org/10.1021/acs.organomet.4c00015
Organometallics 2024, 43, 695−705

This mixed nature is consistent with the observed split into several resolved bands, mostly at longer wavelengths, which appear upon reduction (Figure 4). Second, the sharp peak observed at just above 400 nm in Figures 2 and 4 is probably best described as LMCT from the chloro ligands to the low-lying, partially filled SOMO based on Fe^{III}. This agrees well with the observation that the band is entirely bleached upon filling this orbital by reduction to Fe^{II} (Figure 4).

As noted above, reduction results in the replacement of the triple-peaked LMCT absorption of $[\mathbf{2}]^+$ with two intense bands at 735 and 357 nm in $[\mathbf{2}]^0$. The TD-DFT analysis of $[\mathbf{2'}]^0$ (Figure S14) revealed a transition at 644.40 nm consisting of MLCT from the HOMO − 1 (roughly 42% Fe d_{xz}) to the LUMO ($\pi^*(\alpha$-diimine)), which corresponds to the experimental 735 nm peak. The higher energy band calculated at 327.32 nm is dominated by the MLCT from the HOMO (50% Fe d_{yz}) to the LUMO + 2 ($\pi^*(C_2Ph)$), which corresponds to the experimental 357 nm peak. Both of these agree well with the previous analysis of $[Fe(HMTI)(C_2Ph)_2]^+$ under similar conditions (0.1 M n-Bu_4NPF_6 in THF), except that the MLCT bands in that case appeared at 762 and 336 nm.[26] The differences in transition energies are consistent with the more electron-rich nature of TIM compared to HMTI, as discussed in the Electrochemical Section. HMTI is expected to be slightly more electron-withdrawing, which lowers the energies of the filled Fe d orbitals. While the energies of the C_2Ph-based orbitals remain relatively constant, the gap between the filled dπ and $\pi^*(C_2Ph)$ will increase, resulting in the small blue shift from 357 nm in $[\mathbf{2}]^0$ to 336 nm in $[Fe(HMTI)(C_2Ph)_2]^0$.[26] In contrast, the $\pi^*(\alpha$-diimines)s of HMTI are lower in energy than those of TIM due to the lack of substituents upon the carbon backbone of the former. This difference causes the bathochromic shift of the lower energy MLCT, as is experimentally observed.

The calculated spectra of $[\mathbf{1'}]^0$ correctly predict the growth of a low-energy band at 677.82 nm (Table S7), which matches reasonably well with the observed band at ca. 750 nm (vide supra). This is described as an MLCT transition from the HOMO − 1 (58% Fe d_{xz}) to the LUMO ($\pi^*(\alpha$-diimine)). It is, therefore, analogous in composition to the lowest-energy MLCT transition of $[\mathbf{2'}]^0$ as discussed above. The remaining experimental bands observed at 569 and 491 nm are not well replicated. These are tentatively assigned to a pair of transitions predicted at 407.57 and 379.56 nm, which consist of excitation from the HOMO − 5 and HOMO − 6, respectively, to the LUMO. Both are essentially LLCT transitions from predominantly chloro p orbitals (with minor admixtures of Fe d character) to the $\pi^*(\alpha$-diimine). This would match qualitatively with the discussion of the calculated spectra of $[\mathbf{1'}]^+$ presented above. However, the calculated intensity of the excitation at 407.57 nm is very low, inconsistent with the experimental observation of two relatively intense bands. The calculated transitions are also noticeably higher in energy than the experimental bands. However, no other even moderately intense peaks are predicted above 300 nm (see Figure S11), and thus the experimental peaks at 491 and 569 nm are tentatively assigned to LLCT transitions. The apparent reduction of these distinct experimental bands into a single computed manifold may be a byproduct of the well-known tendency of DFT methods to overdelocalize electron density, artificially convoluting what would be better described as distinct orbitals (and hence distinct electronic transitions).

The TD-DFT analysis of $[\mathbf{1'}]^{-1}$ is somewhat complex. Two dominant bands are observed in the calculated spectrum (Figure S12). The first of these, at 724.77 nm, consists of an excitation from the newly populated α SOMO (π^*(diimine)) to the α LUMO. The latter is composed of the π^*(diimine) of the appropriate symmetry to participate in backbonding with the Fe d_{xz}. Since the α LUMO bears substantial Fe d character (65%), the excitation is of mixed $\pi^*-\pi^*$ and LMCT character. This transition may be assigned to the experimental band centered at 668 nm in Figure 4. The remaining calculated band is quite intense and reasonably narrow, providing an attractive assignment for the experimental band at 527 nm. However, the four predicted excitations ranging from roughly 300 to 330 nm are inconsistent with the experiment. The lowest energy of these (326.42) is best described as a $\pi^*-\pi^*$ from the α SOMO to the α LUMO + 2. While this assignment would logically fit with the observed intense peak at 527 nm, the energetic mismatch suggests that the model of $[\mathbf{1'}]^{-1}$ used here is inadequate for the full explanation of the properties of $[\mathbf{1}]^{-1}$. This deficiency may perhaps be traced to the inherent limitations of the calculation as noted above (e.g., the unphysical spin unrestricted assumption and the tendencies of DFT to overestimate delocalization); however, the spin state of $[\mathbf{1}]^{-1}$ is also assumed and may therefore be incorrect. Lacking any further experimental characterization of $[\mathbf{1}]^{-1}$ beyond SEC, further computational assessment has not been attempted.

CONCLUSIONS

The successful preparation of Fe^{III}(TIM) bis-alkynyl complexes in good yields provides an alternative to Fe(HMTI) analogues for further study of the electronic properties of Fe-tetraimine organometallics. Electronic absorption spectra and voltammetric data indicate that TIM is a more electron-rich macrocycle than HMTI, which results in higher energy dπ orbitals in Fe(TIM) than those in Fe(HMTI). Similar to the previously reported $[Fe(HMTI)(C_2Y)_2]^+$,[27] both $[Fe(TIM)Cl_2]^+$ and $[Fe(TIM)(C_2R)_2]^+$ are low spin d^5 species based on their EPR characteristics. Among many interesting features revealed by SEC analysis is the emergence of the low-energy MLCT band(s) with the concurrent disappearance of the LMCT band(s) upon the first one-electron reduction of both $[\mathbf{1}]^+$ and $[\mathbf{2}]^+$. The key features noted in both electronic absorption spectra and the SEC study are reconciled with TD-DFT analysis. Earlier studies by Reichgott and Rose revealed that Fe(TIM) promotes photoassisted oxidation of methanol.[41] Both potential and underpinning mechanisms of this intriguing finding remain underexplored. Our detailed studies of the optoelectronic properties of $[Fe(TIM)(C_2R)_2]^+$ species provide a foundation for further investigation of the photoactivities of Fe(TIM) organometallics, an ongoing research theme in our laboratory.

EXPERIMENTAL SECTION

Materials. Dry THF was distilled over Na/benzophenone prior to use. n-Butyllithium was purchased from Sigma-Aldrich and used as received. Triisopropylsilylacetylene ($HC_2Si^iPr_3$) and phenylacetylene (HC_2Ph) were purchased from Oakwood Chemical. Triethylsilylacetylene (HC_2SiEt_3) was purchased from GFS Chemicals. $[Fe(TIM)(NCCH_3)_2](PF_6)_2$ was prepared according to literature procedures.[41]

Physical Measurements. UV−vis spectra were obtained with a JASCO V-780 UV−vis−NIR spectrophotometer. Fourier transform infrared (FT-IR) spectra were measured as neat samples using a

https://doi.org/10.1021/acs.organomet.4c00015
Organometallics 2024, 43, 695−705

JASCO FT/IR-6700 spectrometer equipped with a ZnSe ATR accessory. ESI-MS was analyzed on an Advion LC/MS spectrometer. Elemental analyses were performed by Atlantic Microlab, Inc., in Norcross, GA. ^{1}H NMR spectra were recorded on a Varian INOVA 300 NMR spectrometer operating at 300 MHz. Electrochemical analysis was done on a CHI620A voltammetric analyzer with a glassy carbon working electrode (diameter = 2 mm), a Pt-wire auxiliary electrode, and a Ag/AgCl reference electrode. Spectroelectrochemical measurements were performed on a JASCO V-780 UV−vis−NIR spectrophotometer using an optically transparent thin-layer electrochemical (OTTLE) liquid-sample cell with a 0.2 mm optical path length, 0.3 mL sample volume, and a CaF_2 window.[42] The cell was equipped with a mesh Pt working electrode, a mesh Pt auxiliary electrode, and a Ag ($[\mathbf{2}]^+$) or Pt ($[\mathbf{1}]^+$) pseudoreference electrode. The analyte concentration was 5.0 mM for both $[\mathbf{1}]^+$ and $[\mathbf{2}]^+$ in dry CH_2Cl_2 and dry THF, respectively, and at 0.1 M n-Bu_4NPF_6 electrolyte concentration.

Computational Methods. Geometry optimizations of structures $[\mathbf{1}']^+$ and $[\mathbf{2}']^+$ are based on their respective crystal structures, performed using unrestricted open-shell DFT.[40] The basis set 6-31G** was used for all atoms.[43] All calculations were carried out with the Gaussian 16 suite using GaussView, version 6.0.[40,44]

Synthesis of [1]PF$_6$. $[Fe(TIM)(NCCH_3)_2](PF_6)_2$ (1.00 g, 1.48 mmol) was dissolved in 250 mL of acetone. A solution of $FeCl_3$ (527 mg, 3.25 mmol) in acetone (300 mL) was prepared and added dropwise to the starting material over a period of 2 h. The resulting orange solution volume was reduced in vacuo and the addition of diethyl ether produced a yellow solid. The recovered solid was washed with CH_2Cl_2 and hexanes to yield 721 mg of a yellow powder (1.38 mmol, 92% based on $[Fe^{II}(TIM)(NCCH_3)_2](PF_6)_2$). ESI-MS($m/z$): $[\mathbf{1}]^+$, 374.3; visible spectrum, λ_{max} (nm, ε (M^{-1} cm^{-1})): 520 (1200). IR (cm^{-1}): C−H: 2938 (w). CV [$E_{1/2}$/V, ΔE_p/V (vs Fc/Fc$^+$), $i_{p,a}/i_{p,c}$]: $Fe^{III/II}$, −0.36, 0.021, 0.85; $TIM^{0/-1}$, −0.96, 0.11, 0.44.

Synthesis of [2]PF$_6$. Neat $[\mathbf{1}]PF_6$ (154 mg, 0.296 mmol) was dissolved in 5 mL of dry THF and cooled to −78 °C in a dry ice/acetone bath. 0.13 mL of LiC_2Ph cooled to −78 °C (1.2 mmol, prepared from HC_2Ph and excess n-butyllithium in 5 mL of THF) was transferred to a $[\mathbf{1}]PF_6$ flask under N_2. The resulting green solution was held at −78 °C for 2 h prior to exposing it to air. The crude solid was precipitated with hexanes and the recovered solid was washed with CH_2Cl_2 and hexanes. Following recrystallization from acetone and hexanes, complex $[\mathbf{2}]$ PF_6 was isolated as a blue powder in a yield of 85 mg (0.130 mmol, 43% based on $[\mathbf{1}]PF_6$). Elem. anal. found (calcd) for $C_{31}H_{36}N_4FePF_6Cl_2$ ($[\mathbf{2}]PF_6{\cdot}1CH_2Cl_2$): C, 50.21 (50.56); H, 4.98 (4.93); N, 7.44 (7.61). ESI-MS(m/z): $[M]^+$, 506.7; visible spectrum, λ_{max} (nm, ε (M^{-1} cm^{-1})): 671 (4300), 563 (4100), 514 (3900). IR (cm^{-1}): C≡C: 2083 (w). CV [$E_{1/2}$/V, ΔE_p/V (vs Fc/Fc$^+$), $i_{p,a}/i_{p,c}$]: $Fe^{III/II}$, −0.72, 0.066, 0.97.

Synthesis of [3]PF$_6$. Neat $[\mathbf{1}]PF_6$ (165 mg, 0.317 mmol) was suspended in THF (40 mL) and cooled to −78 °C in a dry ice/acetone bath. A solution of LiC_2SiEt_3 (0.18 mL, 1.01 mmol; in 5 mL THF), cooled to −78 °C, was transferred to the $[\mathbf{1}]PF_6$ flask under N_2. The green $[Fe(TIM)(C_2SiEt_3)_2]PF_6$ solution was held at −78 °C for 1.5 h and then warmed to room temperature over a period of 30 min. The solvent volume was minimized under vacuum at room temperature and degassed CH_2Cl_2 (ca. 5 mL) was added to the flask. The crude solid was precipitated with hexanes and the recovered solid was washed with CH_2Cl_2 and hexanes to yield 0.178 g of a crude red solid. The crude solid was further purified over a silica plug by eluting a red fraction with 4:1 DCM/acetone to yield 66 mg of an air-stable red powder (0.090 mmol, 29% based on $[\mathbf{1}]PF_6$). Elem. anal. found (calcd) for $C_{30}H_{54}FeN_4Si_2PF_6O_{0.5}$ ($[\mathbf{3}]PF_6{\bullet}0.5H_2O$): C, 48.9 (48.9); H, 7.37 (7.40); N, 7.47 (7.61). ESI-MS(m/z): $[M]^+$, 582.2; visible spectrum, λ_{max} (nm, ε (M^{-1} cm^{-1})): 551 (5400), 515 (4100), 514 (3900). IR (cm^{-1}): C≡C: 2019 (w). CV [$E_{1/2}$/V, ΔE_p/V (vs Fc/Fc$^+$), $i_{p,a}/i_{p,c}$]: $Fe^{III/II}$, −0.75, 0.061, 0.95.

Synthesis of [4]PF$_6$. Neat $[\mathbf{1}]PF_6$ (167 mg, 0.321 mmol) was suspended in THF (40 mL) and stirred at 40 °C for 2 h. A solution of $LiC_2Si^iPr_3$ (0.22 mL, 0.96 mmol; in 5 mL THF), warmed from 0 to 21 °C, was transferred to the $[\mathbf{1}]PF_6$ flask under N_2. The resulting green solution was held at 21 °C for 1.5 h. The solvent volume was reduced under vacuum at room temperature and degassed CH_2Cl_2 (ca. 5 mL) was added. The crude solid (202 mg) was obtained by precipitating with hexanes. A Celite plug was used to remove insoluble materials (eluting the product with CH_2Cl_2). Subsequent purification was performed using column chromatography. The red band was eluted with 1:15 acetone/CH_2Cl_2 (v/v) from which a pink solid was isolated to obtain a yield of 50 mg (0.061 mmol, 19% based on $[\mathbf{1}]PF_6$). Elem. anal. found (calcd) for $C_{36}H_{68}N_4Si_2FePF_6O$ ($[\mathbf{4}]PF_6{\cdot}1H_2O$): C, 51.9 (52.1); H, 8.07 (8.15); N, 6.55 (6.76). ESI-MS(m/z): $[M]^+$, 666.4; visible spectrum, λ_{max} (nm, ε (M^{-1} cm^{-1})): 558 (6400). IR (cm^{-1}):C≡C: 2020 (m). CV [$E_{1/2}$/V, ΔE_p/V (vs Fc/Fc$^+$), $i_{p,a}/i_{p,c}$]: $Fe^{III/II}$, −0.76, 0.133, 1.03.

X-Ray Crystallographic Analysis. Single crystals of $[\mathbf{1}]PF_6$ and $[\mathbf{2}]PF_6$ were obtained through the slow diffusion of hexanes into a concentrated acetone ($[\mathbf{1}]PF_6$) or chloroform ($[\mathbf{2}]PF_6$) solution. Single crystals of complex $[\mathbf{3}]NTf_2$ were grown through slow diffusion of hexanes into a concentrated acetone solution of $[\mathbf{3}]NTf_2$. A counteranion exchange with potassium bistriflimide ($KNTf_2$) was performed with $[\mathbf{3}]PF_6$ due to difficulties encountered with crystallization using PF_6^- as the counteranion. X-ray diffraction data were obtained on a Bruker QUEST diffractometer with Mo Kα radiation (λ = 0.71073 Å) at 150 K for $[\mathbf{1}]^+$ and $[\mathbf{3}]^+$ and with Cu Kα radiation (λ = 1.54178 Å) at 150 K for $[\mathbf{2}]^+$. Data were collected, reflections were indexed and processed using APEX4,[45] and reduced using SAINT.[46] The space groups were assigned, and the structures were solved by direct methods using XPREP within the SHELXTL suite of programs,[46,47] solved using SHELXT, and refined using SHELXL and ShelXle.[47,48]

■ ASSOCIATED CONTENT

Supporting Information

The Supporting Information is available free of charge at https://pubs.acs.org/doi/10.1021/acs.organomet.4c00015.

Crystallographic details, experimental details, electrochemical data, absorption spectra, IR spectra, ^{1}H NMR spectra, EPR spectra, and selected DFT and TD-DFT data (PDF)

Crystallographic data for $[\mathbf{1}]^+$, $[\mathbf{1}]^0$, $[\mathbf{1}]^{1-}$, $[\mathbf{2}]^+$, and $[\mathbf{2}]^0$ (TXT)

Accession Codes

CCDC 2324420−2324422 contain the supplementary crystallographic data for this paper. These data can be obtained free of charge via www.ccdc.cam.ac.uk/data_request/cif, or by emailing data_request@ccdc.cam.ac.uk, or by contacting The Cambridge Crystallographic Data Centre, 12 Union Road, Cambridge CB2 1EZ, UK; fax: +44 1223 336033.

■ AUTHOR INFORMATION

Corresponding Author

Tong Ren − *Department of Chemistry, Purdue University, West Lafayette, Indiana 47907, United States;* orcid.org/0000-0002-1148-0746; Email: tren@purdue.edu

Authors

Prakhar Gautam − *Department of Chemistry, Purdue University, West Lafayette, Indiana 47907, United States*

Reese A. Clendening − *Department of Chemistry, Purdue University, West Lafayette, Indiana 47907, United States;* Present Address: School of Science and Mathematics, Cedarville University, Cedarville, Ohio, 45314, United States

Andrew T. Poore − *Department of Chemistry, Purdue University, West Lafayette, Indiana 47907, United States*

https://doi.org/10.1021/acs.organomet.4c00015
Organometallics 2024, 43, 695−705

Shiliang Tian − *Department of Chemistry, Purdue University, West Lafayette, Indiana 47907, United States;* orcid.org/0000-0002-9830-5480

Complete contact information is available at: https://pubs.acs.org/10.1021/acs.organomet.4c00015

Notes

The authors declare no competing financial interest.

■ ACKNOWLEDGMENTS

This material was based upon work supported by the U.S. National Science Foundation (CHE 2102049) and by the donors of ACS Petroleum Research Fund under grant no. PRF 66514-ND3. The authors wish to thank Professor Neil Tomson for the advice on the preparation of [Fe(TIM)$(NCCH_3)_2$]$(PF_6)_2$, Professor James H. Davis for providing $KNTf_2$, and Dr. Matthias Zeller for crystallographic consultation.

■ REFERENCES

(1) Tok, G. C.; Reiter, S.; Freiberg, A. T. S.; Reinschlüssel, L.; Gasteiger, H. A.; de Vivie-Riedle, R.; Hess, C. R. H2 Evolution from Electrocatalysts with Redox-Active Ligands: Mechanistic Insights from Theory and Experiment vis-Ã -vis Co-Mabiq. *Inorg. Chem.* **2021**, *60*, 13888−13902.

(2) Esezobor, O. Z.; Zeng, W.; Niederegger, L.; Grübel, M.; Hess, C. R. Co-Mabiq Flies Solo: Light-Driven Markovnikov-Selective C- and N-Alkylation of Indoles and Indazoles without a Cocatalyst. *J. Am. Chem. Soc.* **2022**, *144*, 2994−3004.

(3) Malme, J.; Clendening, R. A.; Ash, R.; Curry, T.; Ren, T.; Vura-Weis, J. Nanosecond Metal-to-Ligand Charge Transfer State in an Fe(II) Chromophore: Lifetime Enhancement via Nested Potentials. *J. Am. Chem. Soc.* **2023**, *145*, 6029−6034.

(4) Baldwin, D. A.; Pfeiffer, R. M.; Reichgott, D. W.; Rose, N. J. Synthesis and Reversible Ligation Studies of New Low-Spin Iron(II) Complexes Containing a Planar Cyclic Tetradentate Ligand and Other Donor Molecules Including Carbon-Monoxide. *J. Am. Chem. Soc.* **1973**, *95*, 5152−5158.

(5) Hess, C. R.; Weyhermuller, T.; Bill, E.; Wieghardt, K. {Fe(tim)}(2): An Fe-Fe Dimer Containing an Unsupported Metal-Metal Bond and Redox-Active N-4 Macrocyclic Ligands. *Angew. Chem., Int. Ed.* **2009**, *48*, 3703−3706.

(6) Hess, C. R.; Weyhermuller, T.; Bill, E.; Wieghardt, K. Influence of the Redox Active Ligand on the Reactivity and Electronic Structure of a Series of Fe(TIM) Complexes. *Inorg. Chem.* **2010**, *49*, 5686−5700.

(7) Tomson, N. C.; Labios, L. A.; Weyhermuller, T.; Figueroa, J. S.; Wieghardt, K. Redox Noninnocence of Nitrosoarene Ligands in Transition Metal Complexes. *Inorg. Chem.* **2011**, *50*, 5763−5776.

(8) Rodriguez Segura, L.; Ren, T. Formation of an Aza-Cobalt-Cyclobutene on CoIII(TIM): Hidden Noninnocence of the TIM Ligand. *Organometallics* **2022**, *41*, 1130−1133.

(9) Rodriguez Segura, L.; Clendening, R. A.; Ren, T. Further Exploration of Aza-Cobalt-Cyclobutenes on CoIII(TIM) Complexes: Reactivity and Spectroelectrochemistry. *Organometallics* **2023**, *42*, 1717−1724.

(10) Long, N. J.; Williams, C. K. Metal Alkynyl Complexes: Synthesis and Materials. *Angew. Chem., Int. Ed.* **2003**, *42*, 2586−2617.

(11) Wong, Y. S.; Paik, H. N.; Chieh, P. C.; Carty, A. J. Two-carbon three-electron ligands. Phosphonium−betaine complexes via nucleophilic attack by phosphites on a σ-π-acetylide di-iron hexacarbonyl derivative. *J. Chem. Soc., Chem. Commun.* **1975**, 309−310.

(12) Smith, W. F.; Taylor, N. J.; Carty, A. J. Acetylene−acetylide coupling via reactions of phosphido-bridged σ−π-acetylides with alkynes. X-Ray crystal structures of $[Fe_2(CO)_5\{PPh_2C(O)C(Bu^t)$-$CC(CO_2Et)C(CO_2Et)\}]$ and $[Fe_2(CO)_5\{PPh_2C(Ph)C(CO_2Et)CC$-$(Bu^t)CO\}]$. *J. Chem. Soc., Chem. Commun.* **1976**, *0*, 896−898.

(13) Bruce, M. I.; Neil Duffy, D.; Liddell, M. J.; Snow, M. R.; Tiekink, E. R. T. Reactions of transition metal σ-acetylide complexes X. Cycloaddition of tetracyanoethene to manganese, iron and nickel complexes, and hydration of a related tungsten complex. X-Ray structures of Fe{C[=C(CN)2]CPh=C(CN)2}(CO)2(η- C5H5) and Ni{C[=C(CN)2]CPh=C(CN)2} (PPh3)(η-C5H5). *J. Organomet. Chem.* **1987**, *335*, 365−378.

(14) Johnson, B. F. G.; Kakkar, A. K.; Khan, M. S.; Lewis, J. Synthesis of Novel Rigid Rod Iron Metal Containing Polyyne Polymers. *J. Organomet. Chem.* **1991**, *409*, C12−C14.

(15) Atherton, Z.; Faulkner, C. W.; Ingham, S. L.; Kakkar, A. K.; Khan, M. S.; Lewis, J.; Long, N. J.; Raithby, P. R. Rigid-Rod Sigma-Acetylide Complexes of Iron, Ruthenium and Osmium. *J. Organomet. Chem.* **1993**, *462*, 265−270.

(16) Paul, F.; Lapinte, C. Organometallic Molecular Wires and Other Nanoscale-sized Devices. An Approach using the Organoiron (dppe)Cp*Fe Building Block. *Coord. Chem. Rev.* **1998**, *178*−*180*, 431−509.

(17) Halet, J. F.; Lapinte, C. Charge delocalization vs localization in carbon-rich iron mixed-valence complexes: A subtle interplay between the carbon spacer and the (dppe)Cp*Fe organometallic electrophore. *Coord. Chem. Rev.* **2013**, *257*, 1584−1613.

(18) Lissel, F.; Schwarz, F.; Blacque, O.; Riel, H.; Lortscher, E.; Venkatesan, K.; Berke, H. Organometallic Single-Molecule Electronics: Tuning Electron Transport through X(diphosphine)(2)-FeC4Fe(diphosphine)(2)X Building Blocks by Varying the Fe-X-Au Anchoring Scheme from Coordinative to Covalent. *J. Am. Chem. Soc.* **2014**, *136*, 14560−14569.

(19) Bhutto, S. M.; Mercado, B. Q.; Holland, P. L. Dinitrogen Binding and Functionalization from a Low-Coordinate Alkynyliron Complex. *Inorg. Chem.* **2023**, *62*, 9335−9342.

(20) Richards, C. A.; Rath, N. P.; Neely, J. M. Iron-Catalyzed Alkyne Carboamination via an Isolable Iron Imide Complex. *Organometallics* **2021**, *40*, 2945−2950.

(21) Deng, Y.; Wei, X.-J.; Wang, X.; Sun, Y.; Noël, T. Iron-Catalyzed Cross-Coupling of Alkynyl and Styrenyl Chlorides with Alkyl Grignard Reagents in Batch and Flow. *Chem.—Eur. J.* **2019**, *25*, 14532−14535.

(22) Banziger, S. D.; Ren, T. Syntheses, Structures and Bonding of 3d Metal Alkynyl Complexes of Cyclam and Its Derivatives. *J. Organomet. Chem.* **2019**, *885*, 39−48.

(23) Ren, T. Sustainable metal alkynyl chemistry: 3d metals and polyaza macrocyclic ligands. *Chem. Commun.* **2016**, *52*, 3271−3279.

(24) Mash, B. L.; Yang, Y.; Ren, T. Improving Redox Reversibility and Intermetallic Coupling of Co(III) Alkynyls through Tuning of Frontier Orbitals. *Organometallics* **2020**, *39*, 2019−2025.

(25) Clendening, R. A.; Ren, T. Mono- and Bis-alkynyl Iron Complexes Supported by a "Softened" Tetraaza Macrocycle. *Eur. J. Inorg. Chem.* **2022**, *2022*, No. e202101021.

(26) Clendening, R. A.; Zeller, M.; Ren, T. Bis-Alkynyl Complexes of Fe(III) Tetraaza Macrocycles - A Tale of Two Rings. *Inorg. Chem.* **2022**, *61*, 13442−13452.

(27) Clendening, R. A.; Delancey, S. S.; Poore, A. T.; Xue, S.; Guo, Y.; Tian, S.; Ren, T. Enabling Valence Delocalization in Iron (III) Macrocyclic Complexes through Ring Unsaturation. *Inorg. Chem.* **2023**, *62*, 11121−11133.

(28) Clendening, R. A. One Macrocyclic Ring to Rule the Iron: Harnessing Macrocyclic Unsaturation to Tune the Properties of Organometallic Complexes. Ph.D Thesis; Purdue University, 2023.

(29) Maroney, M.; Fey, E.; Baldwin, D.; Stenkamp, R.; Jensen, L.; Rose, N. Bonding mode of axial thiocyanate ligands of iron macrocyclic complexes. Crystal structure of [Fe (TIM)(SCN) 2] PF6. *Inorg. Chem.* **1986**, *25*, 1409−1414.

(30) Rodriguez Segura, L.; Lee, S. A.; Mash, B. L.; Schuman, A. J.; Ren, T. A Series of Mono-and Bis-Alkynyl Co (III) Complexes Supported by a Tetra-imine Macrocyclic Ligand (TIM). *Organometallics* **2021**, *40*, 3313−3322.

(31) Cordero, B.; Gomez, V.; Platero-Prats, A. E.; Reves, M.; Echeverria, J.; Cremades, E.; Barragan, F.; Alvarez, S. Covalent radii revisited. *Dalton Trans.* **2008**, *21*, 2832−2838.
(32) Cao, Z.; Forrest, W. P.; Gao, Y.; Fanwick, P. E.; Ren, T. *trans*-$[Fe(cyclam)(C_2R)_2]^+$: A New Family of Iron(III) Bis-Alkynyl Compounds. *Organometallics* **2012**, *31*, 6199−6206.
(33) Stoll, S.; Schweiger, A. EasySpin, a comprehensive software package for spectral simulation and analysis in EPR. *J. Magn. Reson.* **2006**, *178*, 42−55.
(34) Stolzenberg, A. M.; Strauss, S. H.; Holm, R. Iron (II, III)-chlorin and-isobacteriochlorin complexes. Models of the heme prosthetic groups in nitrite and sulfite reductases: means of formation and spectroscopic and redox properties. *J. Am. Chem. Soc.* **1981**, *103*, 4763−4778.
(35) Safo, M. K.; Gupta, G. P.; Watson, C. T.; Simonis, U.; Walker, F. A.; Scheidt, W. R. Models of the cytochromes b. Low-spin bis-ligated (porphinato)iron(III) complexes with unusual molecular structures and NMR, EPR, and Moessbauer spectra. *J. Am. Chem. Soc.* **1992**, *114*, 7066−7075.
(36) Watson, C. T.; Cai, S.; Shokhirev, N. V.; Walker, F. A. NMR and EPR Studies of Low-Spin Fe(III) Complexes of meso-Tetra-(2,6-Disubstituted Phenyl)Porphyrinates Complexed to Imidazoles and Pyridines of Widely Differing Basicities. *Inorg. Chem.* **2005**, *44*, 7468−7484.
(37) Walker, F. A.; Nasri, H.; Turowska-Tyrk, I.; Mohanrao, K.; Watson, C. T.; Shokhirev, N. V.; Debrunner, P. G.; Scheidt, W. R. π-Acid Ligands in Iron(III) Porphyrinates. Characterization of Low-Spin Bis(*tert*-butylisocyanide)(porphyrinato)iron(III) Complexes Having $(d_{xz},d_{yz})^4(d_{xy})^1$ Ground States. *J. Am. Chem. Soc.* **1996**, *118*, 12109−12118.
(38) Griffith, J. S. Binding in Hæmoglobin Azide as Determined by Electron Resonance: Theory of Electron Resonance in Ferrihæmoglobin Azide. *Nature* **1957**, *180*, 30−31.
(39) Griffith, J. S. Theory of Epr in Low-Spin Ferric Haemoproteins. *Mol. Phys.* **1971**, *21*, 135−139.
(40) Frisch, M. J.; Trucks, G. W.; Schlegel, H. B.; Scuseria, G. E.; Robb, M. A.; Cheeseman, J. R.; Scalmani, G.; Barone, V.; Petersson, G. A.; Nakatsuji, H.; et al. *Gaussian 16* Rev. A.03; Gaussian Inc.: Wallingford, CT, 2016.
(41) Reichgott, D. W.; Rose, N. J. Photoassisted oxidation of methanol catalyzed by a macrocyclic iron complex. *J. Am. Chem. Soc.* **1977**, *99*, 1813−1818.
(42) Krejcik, M.; Danek, M.; Hartl, F. Simple construction of an infrared optically transparent thin-layer electrochemical cell: Applications to the redox reactions of ferrocene, Mn2(CO)10 and Mn(CO)3(3,5-di-t-butyl-catecholate). *J. Electroanal. Chem. Interfacial Electrochem.* **1991**, *317*, 179−187.
(43) Rassolov, V. A.; Pople, J. A.; Ratner, M. A.; Windus, T. L. 6-31G* basis set for atoms K through Zn. *J. Chem. Phys.* **1998**, *109*, 1223−1229.
(44) Dennington, R.; Keith, T. A.; Millam, J. M. *GaussView* 6.0. 16.; Semichem Inc.: Shawnee Mission, KS, USA, 2016; pp 143−150.
(45) Bruker. *APEX4 v2022.10−1*, Saint V8.40B; Bruker AXS, Inc.: Madison, WI, 2022.
(46) Bruker. *SHELXTL Suite of Programs*, version 6.14; Bruker AXS Inc.: Madison, WI, 2000−2003.
(47) Hübschle, C. B.; Sheldrick, G. M.; Dittrich, B. ShelXle: a Qt graphical user interface for SHELXL. *J. Appl. Crystallogr.* **2011**, *44*, 1281−1284.
(48) Sheldrick, G. M. Crystal structure refinement with SHELXL. *Acta Crystallogr., Sect. C: Struct. Chem.* **2015**, *71*, 3−8.

https://doi.org/10.1021/acs.organomet.4c00015
Organometallics 2024, 43, 695−705